Characterization of a Plasma Ion Source and of Ion Assisted Deposited Optical Thin Films

Dale E. Morton* and O. Faruk Farsakoglu**

Key words: IAD, Plasma Sources, Ion Guns, Ion Assisted Deposition, Optical Properties.

ABSTRACT

It is well known that IAD (ion assisted deposition) using a plasma source improves the optical and physical characteristics of optical thin films. There are many types of plasma sources. The broad beam CC-105 "cold cathode" plasma source is a small versatile ion source that is easily retrofitted into existing deposition chambers or new installations. This paper discusses characterization of the ion produced by the plasma source and the properties of thin films produced using the plasma source for IAD (ion assisted deposition).

INTRODUCTION

Considerable data has been generated and reported on the use of various types of ion guns[1] for pre-cleaning substrates and as IAD in depositing optical thin films over the last 15 years.[2,3,4] There is now a plethora of ion sources available for use as well as many "improvements" on older designs. Thus it is necessary to continue making and publishing studies on what may seem like old hat material. This paper is written in two parts; the first part summarizes techniques used to characterize the ions produced by the CC-105 and the second part reports on recent work done using a cold cathode source for IAD in depositing several materials. These studies were conducted on single layer films but we also describe some results for multi-layer coating stacks deposited on mineral and polymer substrates. Traditional glow discharge in-situ pre-cleaning steps were effective in some situations, but not all. An O_2 glow discharge would be effective at burning off hydrocarbons while a freon (often used in the semiconductor industry) would etch germanium, silicon or silica based surfaces. The advent of the ion gun gave a cleaning tool that was equally effective (or probably even better) than the glow discharge and it was nondiscriminatory. High energy ion bombardment of the surface would etch or mill the surface removing both contaminants and some of the surface molecules leaving a nascent surface to begin deposition.[5,6]

IAD can be done with an inert gas (Ar) or with a reactive gas (O_2) or a mixture of the two. Early work was done with a Kaufman type hot cathode which could operate effectively with Ar but but would burn out in pure oxygen and have reduced life in mixtures. Thus the early studies were heavily weighted towards Ar bombardment and studying the optical and physical densification of the films.[2,7] The densification of the films results in higher refractive indexes and greater moisture stability.[3,8,9] Work has been done with both low[2,3,8] and high[2,3,9] energy bombardment. The lighter anion molecules such as Al_2O_3 and SiO_2 show improved density up to very high energy bombardment levels (300 ev to 1000 ev) whereas the heavier anion molecules such as Ta_2O_5, ZrO2 and TiO_2 are often damaged (preferential sputtering away of O_2 leaving them absorbing) if exposed to energy levels which are too high.[2,9,10]

The cold cathode CC-105 plasma source advantage is that it will run almost continuously in pure oxygen. In fact, this type of ion gun works equally well in oxygen or argon. Appropriate adjustment of system parameters allows for controlling the energy of the impinging ion from about 100 ev to 300 ev or higher.

CHARACTERIZATION OF THE ION SOURCE

The operational characteristics of the ion source were determined using an Integrity®-29 (I-29) fully automated ophthalmic cryo-pumped coating chamber equipped with resistive sources, a 6-pocket E-gun, quartz crystal rate/thickness controller, 3 kW quartz lamp heater and a cryogenically cooled Meissner surface. Internal fixturing consists of a domed calotte, a curved uniformity mask below the calotte which has a quartz crystal mounted in it, an electron beam-gun with the deposition pocket centered in the chamber and a cold cathode ion source (Denton Vacuum CC-105) 8 inches off-center position, pointing straight up. The general equipment arrangement is shown in Figure 1.

Ion Energy Measurements

Ion energy measurements were made using a versatile multi-grid retarding field ion energy analyzer (see Figure 2) (IEA) for the determination of ion energy distribution

---

* Denton Vacuum LLC, 1259 North Church Street, Moorestown, NJ 08057 Phone: 609-439-9100, FAX: 609-439-9111, E-mail: dmorton@dentonvacuum.com.

**Logistics Command, Technical Management Department, K. K. Lojistik K. ligi, 06100 Gumusdere Ankara Turkey. Phone: 0090 312 3845370 ext 2533, FAX: 0090 312 3422031, E-mail: ffarsakoglu@hotmail.com.

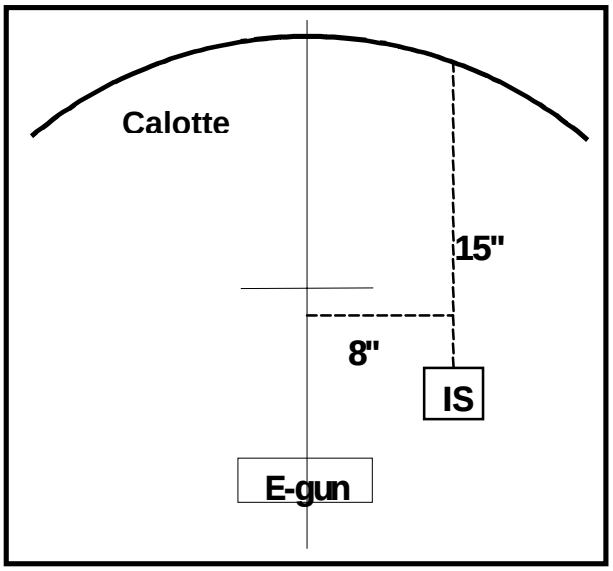

Figure 1. I-29® chamber showing relative location of ion source, E-gun and calotte.

functions (IEDFs) in vacuum processing systems. This study was published previously[11] and is discussed briefly here. The calotte was removed from the chamber and was replaced by a bracket directly above the source. The bracket was designed for mounting the analyzer on one of three plates allowing for measuring ions arriving at angle of 0°, 22.5° and 45° incidence with respect to the ion source axis. Data was taken for three gases; Ar, O_2 and N_2 and for pressures ranging from $1x10^{-4}$ to $4x10^{-4}$ Torr in $1x10^{-4}$ Torr increments.

The IEDFs were measured with a retarding field, three-grid ion energy analyzer[12] illustrated in Figure 2. For the pressure range used in this work no differential pumping was necessary. The IEDFs were obtained by derivation of the $I(V_s)$ characteristic, where I is the collector current (see Figure 2) and V_s is the scanning potential (both of them were controlled by a computer)[12]. Energy resolution of the IEA is about 2 eV.

Typical IEDFs, measured for three frequently used gases, namely argon, nitrogen, and oxygen, at the same pressure of 0.3 mTorr and D_I = 2 A are shown in Figure 3. Depending on the gas nature, the distributions exhibit different shapes. One should keep in mind that the process conditions for each gas slightly varied: in the case of argon, a lower drive voltage, 115 V, is applied, compared to 155 V for oxygen and nitrogen, as a consequence of a higher ionization rate in argon compared to molecular gases. On the other hand, in the case of nitrogen and oxygen all external parameters were

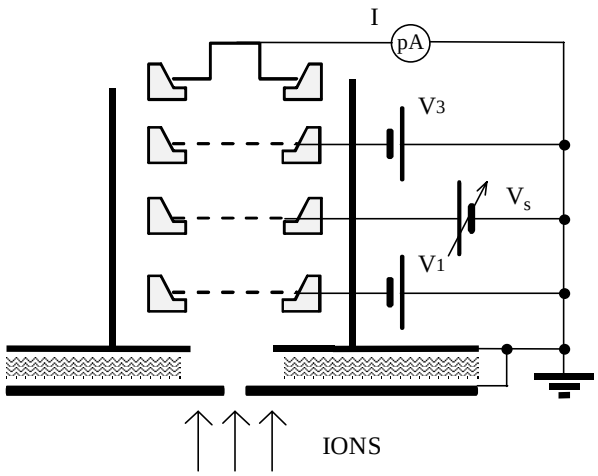

Figure 2. Schematic representation of ion energy analyzer.

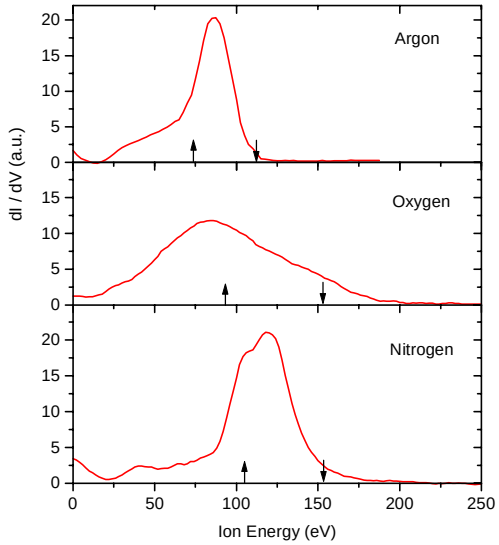

Figure 3. IEDFs measured for different working gases. D_I is 2 A, pressure is $3x10^{-4}$ Torr and the angle from the source axis is 22.5° for all presented curves. Here, and in all other IEDFs in this article, upward and downward pointing arrows indicate $<E_i>$ and V_D respectively.

almost identical; nevertheless, the IEDF for oxygen is much broader and it is shifted to lower energies. This difference can be attributed to negative ion formation in oxygen plasma that changes the plasma potential distribution in the source. Access to the IEDF allowed us to evaluate for each set of experimental conditions an important process parameter, namely the mean ion energy, $\langle E_i \rangle$, using the following expression:

$$\langle E_i \rangle = \frac{\int E \cdot f_i(E) dE}{\int f_i(E) dE}. \qquad 1)$$

Here $f_i(E)$ represents the specific IEDF.

Since oxygen is frequently used in the fabrication process of optical coatings, we particularly focused on the ion characteristics in this gas. Figure 4 represents the IEDFs for oxygen at a pressure of 0.2 mTorr but at different D_I values.

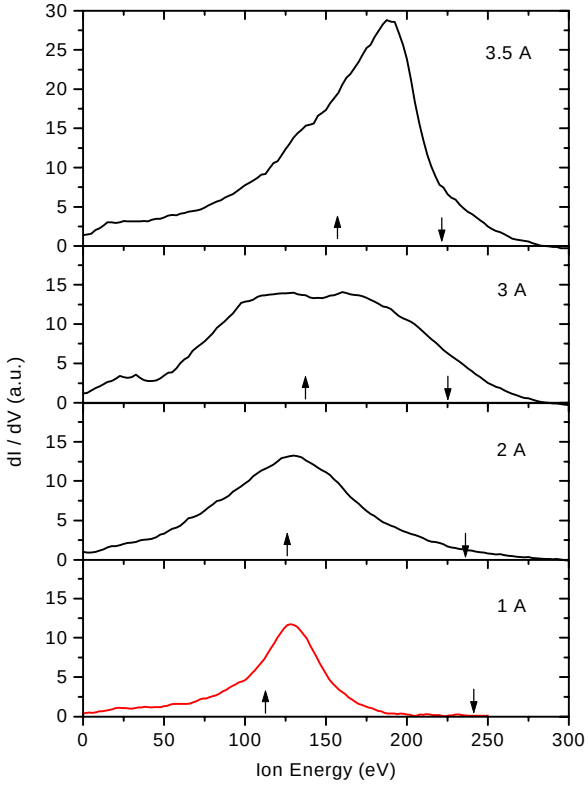

Figure 4. IEDFs for different D_I values at an oxygen pressures of $2x10^{-4}$ Torr.

Increasing D_I leads to broadening of the IEDF, while the ion current density increases substantially. $\langle E_i \rangle$ is shown in Figure 5 as a function of D_I for different angles with respect to the source axis. $\langle E_i \rangle$ values monotonically increase; less variation in $\langle E_i \rangle$ was observed for D_I between 1.5 and 2.5 A. We conclude that the drive current allows one to control the ion flux during deposition while keeping the mean ion energy essentially the same. The IEDFs measured for different angles with respect to the ion source axis yield $\langle E_i \rangle$ values and intensities very close to each other, which confirms a beam uniformity of about 10% over the measured area (~0.5 m^2) assuming axial symmetry.

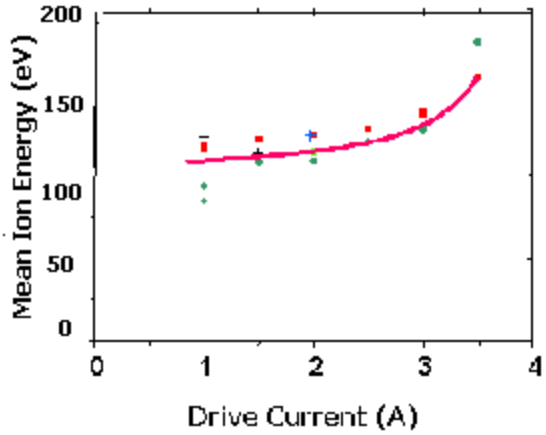

Figure 5. Mean ion energies as a function of drive current for different angles with respect to ion source axis: triangles - O^o, squares – 22.5^o and circles – 45^o.

The effect of pressure on the IEDFs of oxygen ions is shown in Fig. 6. Two effects are observed to occur when the

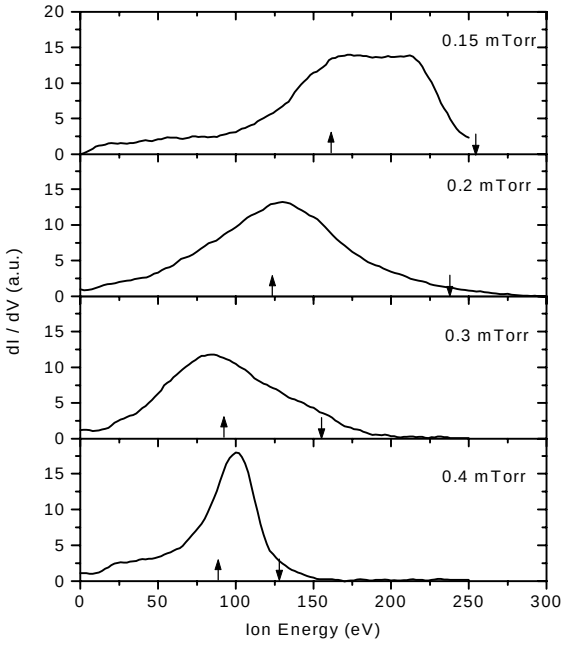

Figure 6. IEDFs for different oxygen pressure values at D_I=2 A.

pressure increases: (i) the drive voltage decreases leading to the observed drop in $\langle E_i \rangle$ as illustrated in Figure 7; (ii) the ion current (area under the curves) drops, in agreement with the Child-Langmuir law ($I \propto U^{3/2}$). It is believed that this effect interferes with changes in the shape of the plasma edge, from which the ions are extracted (plasma expansion at lower pressure). In contrast to nitrogen ions[13] no IEDF broadening due to ion-neutral collisions has been observed here.

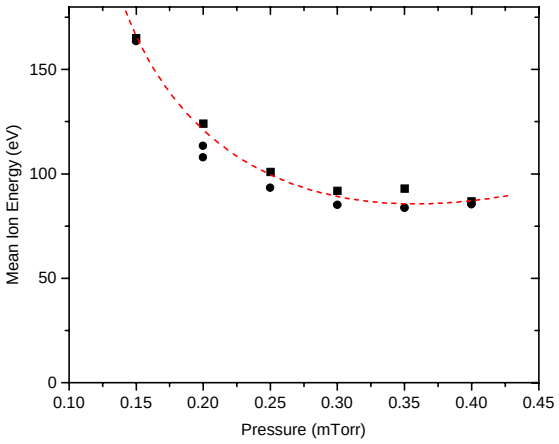

Figure 7. Mean ion energy as a function of pressure for different angles with respect to ion source axis: squares – 22.5° and circles – 45°.

In the case of oxygen, IEDFs are narrower, which may also be attributed to geometrical changes of the extraction zone. It is intuitively expected that V_D is a parameter most closely related to the ion energy. Indeed, as one can see in Fig. 8, the $\langle E_i \rangle$ values derived from almost all IEDFs obtained over a large range of drive currents (0.5-4 A) and gas pressures

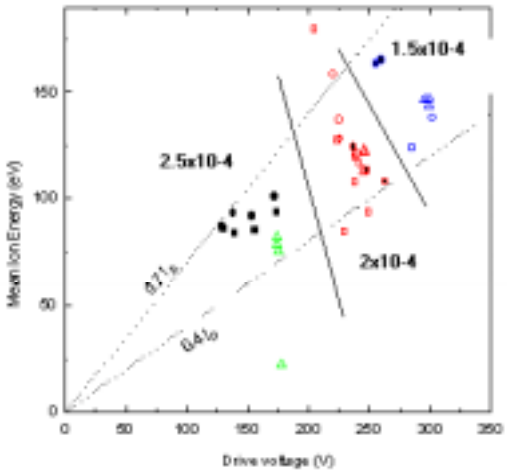

Figure 8. Mean ion energy as a function of drive voltage for different angles with respect to ion source axis: triangles-O°, squares-22.5° and circles-45°.

(1.5-4.0·10^{-4} Torr) lie between $0.4 \cdot eV_D$ and $0.7 \cdot eV_D$. Therefore, a value of $0.5 \cdot eV_D$ can serve as a good approximation of $\langle E_i \rangle$ for the ion source studied in this work. This plot also has the data separated by pressure showing the increased energy at lower pressures.

We cannot distinguish either single- or double-charged ions, or ions with different masses. This lack of information somewhat complicates the interpretation of the IEDFs in molecular gases. Presence of ions with higher energies than those corresponding to the drive voltage (see Figures 3, 4, and 6), points to charge transfer in which double-charged and molecular ions can participate. Recent mass-resolved measurements of IEDFs in nitrogen rf and MW plasmas clearly prove this statement[14].

Ion Current Density Measurements

The density and quality of films formed using IAD are directly related to the ICD (ion current density) used during deposition. The ICD will be related to the drive voltages that are related to the type of gas being used in the ion source, the pressure and the pumping speed of the system. Increasing drive voltage and thus higher ion energies as a function of lower pressure was shown in Figure 8. Another example of this is shown for oxygen in Figure 9 where the drive voltage is shown as a function of the drive current for pressure levels from 1x10^{-4} to 5x10^{-4} Torr in 1x10^{-4} Torr increments. There is a threshold level of pressure required to sustain the plasma. Thus, at 1x10^{-4} Torr, we were unable to sustain the plasma at drive currents above 1.75 amp. At the higher pressures we were able to run the ion source over the entire current range of the drive power supply (0-3.5 amp). Also note that there is very little voltage change required to sustain the plasma at all the higher pressure levels. However, as we will show later, the pressure used during deposition is an important factor in film formation.

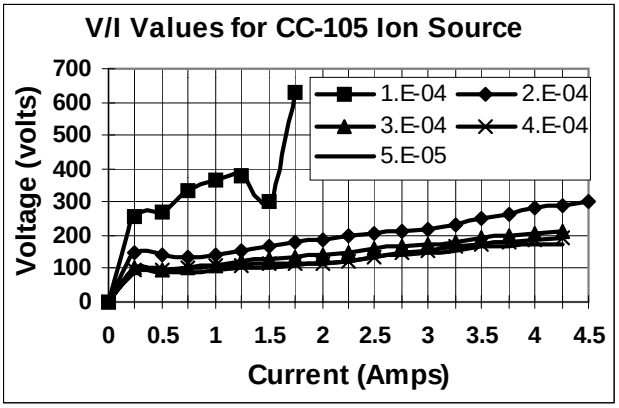

Figure 9. Drive Voltage vs. Drive current for CC-105 operating at various oxygen pressure levels in a 1500 l/sec pumping system.

The ion current densities were measured by mounting a Faraday probe at various positions. A schematic of the probe and the circuitry used for this study is shown in Figure 10. The probe is biased –30 volts to reject any

electrons present and to collect the ions (Note: as recommended by McNeil[15]).

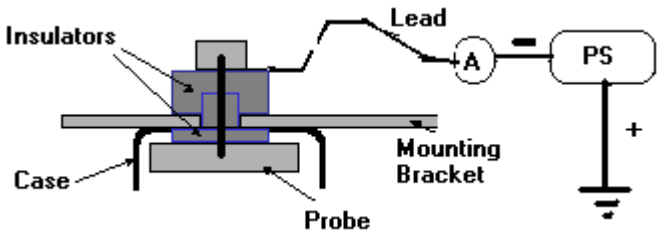

Figure 10. ICD probe and circuitry.

Therefore a study was made of the ICD of the ion source with Faraday probes mounted above the ion source. The first set of ICD measurements were made with 6 probes mounted in a line on 5 cm centers with the first probe mounted on axis 40 cm above the ion source. Again measurements were made for pressure levels from $1x10^{-4}$ to $5x10^{-4}$ Torr in $1x10^{-4}$ Torr increments. Data is shown for Drive current levels of 1-4 amp (Figures 11-14, respectively). These measurements are indicative of the ICD level pattern above the source.

In order to achieve thickness uniformity during deposition, parts being coated are being translated about in the system by some type of a carrier; flat calotte, domed calotte or planetary. Therefore, during deposition, the parts are moving throughout the chamber receiving a continuously varying ICD dose. The film properties are the result of the

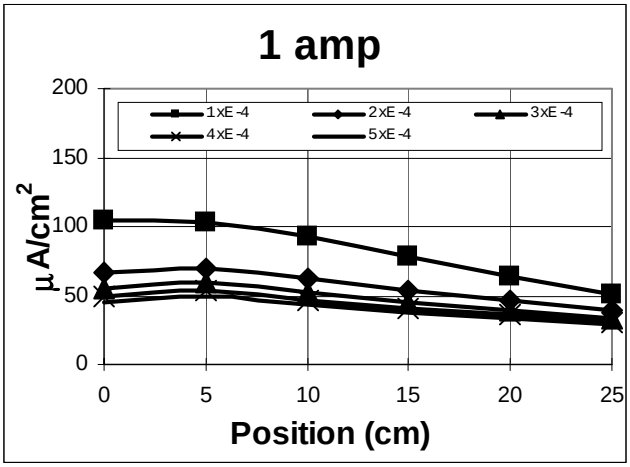

Figure 11. ICD for 1 amp drive current.

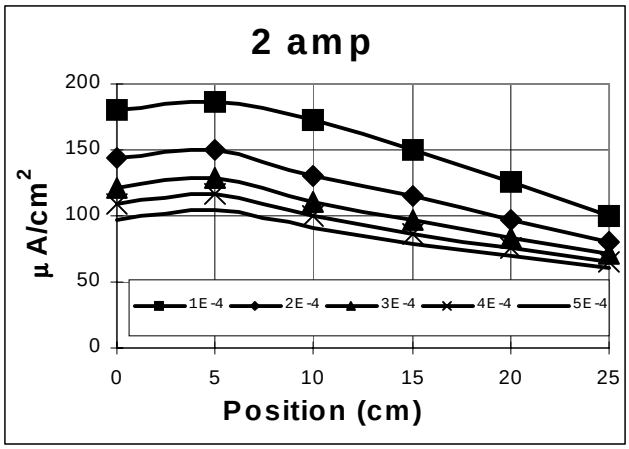

Figure 12. ICD for 2 amp drive current.

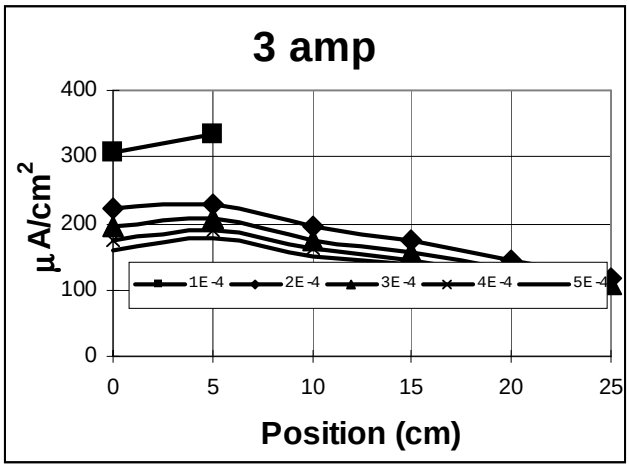

Figure 13. ICD for 3 amp drive current.

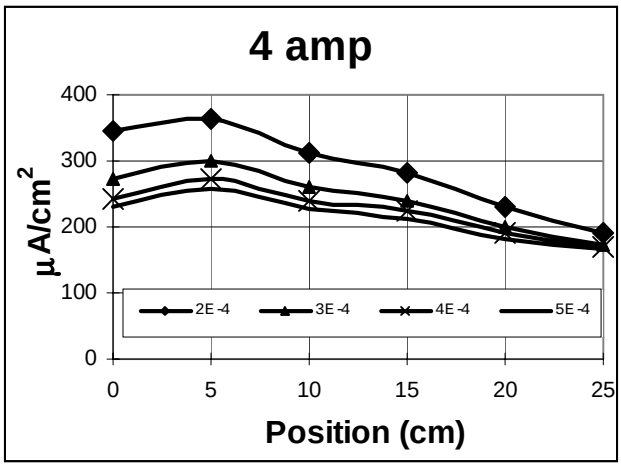

Figure 14. ICD for 4 amp drive current.

sum of all the varying ICD doses, impingement rates and angles of incidence for the molecules and reactivity with the gases in the system as the samples rotate through the system. The only way to gauge the effectiveness of the ICD is to vary parameters during deposition and characterize the resulting films. The data shown in Figures 11 – 14 defines the ICD levels above the ion source but does not clearly represent the distribution during a coating operation.

Therefore, we made another set of measurements to better gauge the ICD exposure during deposition (reported previously[16] and summarized here-in). The six probes were mounted around the outer edge of a domed calotte [see Figure 15]. Position 3 is almost directly above the ion source but at a larger radius. ICD values were then taken as for the linear probe arrangement.

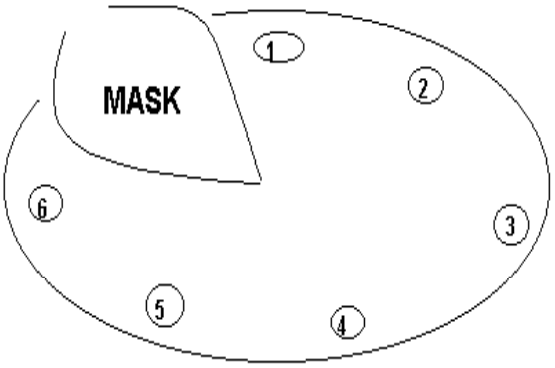

Figure 15. Faraday probes mounted in calotte. Position # 3 is almost directly above the ion source.

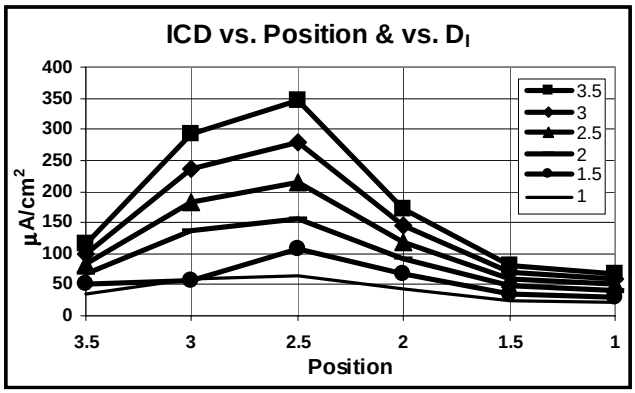

Figure 16. ICD for $2x10^{-4}$ Torr O_2 with drive currents as shown in legend. Average ICD levels are 179, 148, 118 89.7 57.5 and 40.7 μA/cm^2 in order of decreasing drive current.

ICD data for the $2x10^{-4}$ Torr pressure level is shown in Figure 16. This pressure level was chosen since it is the value most commonly used to make low absorbing, high index and moisture stable films.

The next step in the study was to deposit a variety of films using various IAD parameters. These films were characterized by making spectral measurements of the films and extracting the optical coefficients.

DETERMINING OPTICAL COEFFICIENTS

Analysis consisted of measuring the transmittance of coated clear microscope slides and reflectance (at 6^o incidence) of the frosted back microscope slides. From the spectral data the refractive index was calculated from the reflectance using:

$$n_\lambda = \left[n_s \bullet \frac{\left(1 \pm \sqrt{R_\lambda}\right)}{\left(1 \mp \sqrt{R_\lambda}\right)} \right]^{0.5} \qquad (2)$$

where: n_λ is the refractive index at λ
n_s is the refractive index of the substrate
λ wavelength for an odd order in the interference pattern
R_λ Reflectance at λ

The extinction coefficient k_λ was calculated from the reflectance and the transmittance data using a relationship given by Macleod[17]:

$$k_\lambda = \frac{\lambda \bullet (1 - T_\lambda - R_\lambda)}{2\pi \bullet d_m \bullet \left(\frac{n_s^2 + n_f}{n_s \bullet n_f^2} \right)} \qquad (3)$$

Where $\boldsymbol{T_\lambda}$ has been corrected to first surface transmittance

Film thickness (d_m) was measured using a profilometer and/or was calculated from the interference pattern and the index of the materials using:

$$d_m = \frac{m \bullet \lambda}{4 \bullet n_\lambda} \qquad (4)$$

Where d_m is the thickness calculated at the m order in the interference pattern.

At wavelengths where the film is non-absorbing, this calculation results in thickness that is within the accuracy of

the measurements being made. Typically the calculated thickness was the same for each order in the interference pattern unless the film was absorbing. Thus the thickness calculation at all the orders also became a good indicator of when the film was becoming absorbing.

If the film is absorbing, then the refractive index needs to be corrected using the relationship (5):

$$N_\lambda = n_\lambda + \left(\frac{\pi \bullet k_\lambda \bullet d}{\lambda}\right)\left(\frac{1+\sqrt{R_\lambda}}{1-\sqrt{R_\lambda}} - n_s\right) \quad (5)$$

Where N_λ is the corrected refractive index and the conditions for determining the relationship are the same as for equation 3. However, in this case the thickness of the film calculated from a longer wavelength non-absorbing region is used.

The corrected refractive index data is then used to calculate a Hartman type dispersion relationship to be used in comparing films prepared under varying conditions:

$$N_\lambda = A + \frac{B}{(\lambda - C)^2} \quad (6)$$

Where A, B and C are coefficients determined for data over the visible spectral region.

IAD DEPOSITION OF FILMS

We studied the effect of ion energy and ion flux on the refractive index, the deposition rate and the internal stress of TiO_2 and Ta_2O_5 films deposited on silicon wafers and microscope slides. The effect of ion bombardment on the evolution of the film microstructure can be described by a single parameter, E_p, namely the energy delivered to the film per deposited atom:

$$E_p = \langle E_i \rangle \cdot \Phi_i / \Phi_n \quad (7)$$

Here Φ_i is the ion flux and Φ_n is the flux of condensing atoms. Equation 7 is a simplified version of a more complex description of ion-assisted phenomena[18].

Evolution of the TiO_2 and Ta_2O_5 film characteristics as deposited on silicon is shown plotted in Figure 17 as a function of E_p. The results indicate that the deposition rate for both films decreases with E_p as a consequence of densification at higher energy fluxes toward the film. The stress is relatively low (0 - 200 MPa), and it is tensile (positive values) for lower E_p values, while one measurement suggests its conversion to a compressive one (negative value). The effect of E_p appears to be more significant on the evolution of index values for TiO_2 than for Ta_2O_5. TiO_2 is therefore more sensitive to the E_p variations in the present range of conditions, in agreement with the structure-zone model[19,20].

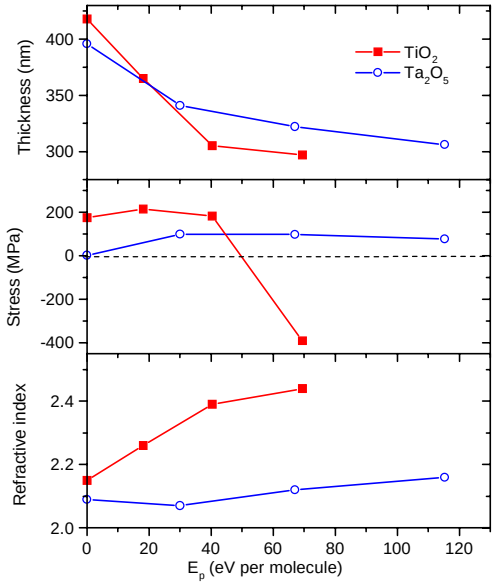

Figure 17. Film characteristics as a function of total ion energy per deposited molecule.

As indicated, we also obtained the optical properties from films deposited on glass (microscope slides). Ta_2O_5 (tantala) films were deposited using various drive currents. Films were prepared at 120°C substrate temperature and 6 Å/sec with chamber pressures of approximately $2x10^{-4}$ Torr for drive currents ranging from 1 ampere to 3 amperes in 0.5 ampere increments. The data for the films is reported in Table I. D_I is the drive current during deposition of the films, ICD_{avg} is the average ion current density ($\mu A/cm^2$) around the calotte, n_{560} is the refractive index at 560 nm, $k_{3\lambda/4}$ is the extinction coefficient at 560 nm and $\Delta n_{3\lambda/4}$ is the shift in the refractive index at the $3\lambda/4$ peak (~1000±50 nm for all of the films) of the film. Δn is calculated from the change in the $3\lambda/4$ transmission minimua. The films become progressively more moisture stable and the refractive index of the films increases as the ion current density exposure increases. A non-IAD film prepared by the preceding parameters was so absorbing that it was not possible to obtain reasonable optical parameters. However, fairly good non-IAD data (still somewhat absorbing) was obtained from samples deposited at higher pressures ($3.5x10^{-4}$ Torr) and a lower deposition rate (3 Å/sec).

Table I.
Ta_2O_5 Film Data

#	D_I	ICD_{avg}	n_{560}	k_{560}	$\Delta n_{3\lambda/4}$
non	0	0	2.041	$\sim 10^{-3}$	-0.044
95	1	41	2.168	0.0003	-0.015
81	2	90	2.129	$<10^{-4}$	-0.005
92	2	90	2.178	$\sim 10^{-4}$	-0.009
86	2.5	118	2.119	0	-0.013
78	3	148	2.179	0	0

The ion current density profiles for the Ta_2O_5 films are the same as shown in Figure 16 since the pressure required to make these films was the same as was used in taking that data ($2x10^{-4}$ Torr). The middle column (n_{560}) shows the increasing index of the films as the ICD is increased and the last column in the Table shows the change in index of the films when measured wet and dry. A zero value for the index change indicates that the film is moisture stable. This measurement was made by immersing the film in water for a while, drying the surface of surface water, making a transmission scan, purging the sample chamber with dry nitrogen for 30 minutes and repeating the transmission scan. Samples determined to be moisture stable were submitted to two other coating houses using other methods to determine moisture stability. They confirmed that these samples were moisture stable.

A plot of the Ta_2O_5 moisture stability vs. the O_2 ion current density is shown in Figure 18. The Δn of -0.007 shown for the film prepared while being exposed to 90 $\mu A/cm^2$ ion current density is the average of the values obtained for runs 81 and 92. The data for run # 86 seems to be out of sync with the rest of the data. This also shows up again when comparing the refractive index data. The films are moisture stable when the average ICD $\geq$ 148 $\mu A/cm^2$.

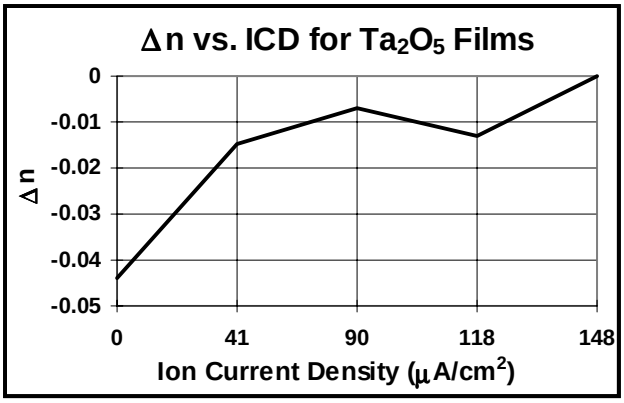

Figure 18. Moisture stability for tantala (Ta_2O_5) films.

Unlike Ta_2O_5, TiO_2 films deposit with a strong gettering action. That is, although the IAD oxygen gas flow is set to achieve a pressure of $2x10^{-4}$ Torr, during the deposition enough of the oxygen combines with the oxygen deficient films so that the pressure is reduced to $1.6x10^{-4}$ Torr. This reduction in pressure causes the ion source drive voltage to increase to maintain the ion current and results in a higher ICD level for a given drive current. This is shown in Figure 19 where the ICD levels vs. drive current are plotted for a chamber pressure of $1.6x10^{-4}$ Torr.

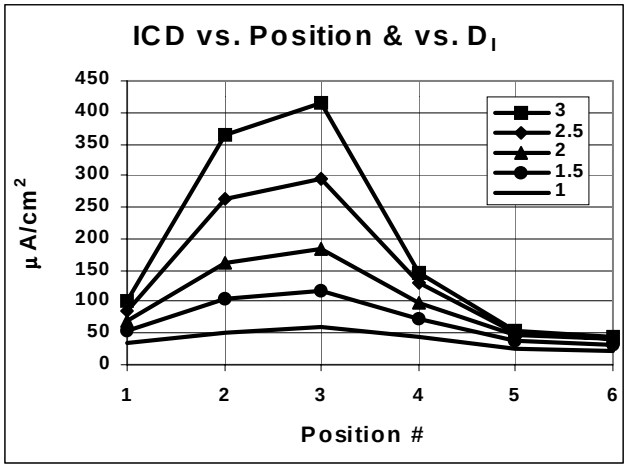

Figure 19. ICD for $1.6x10^{-4}$ Torr O_2 with drive currents as shown in legend. Average ICD levels are 187, 145, 101 69.4 and 39.7 $\mu A/cm^2$ in order of decreasing drive current.

A set of TiO_2 (titania) films were prepared at 40°C substrate temperature and 3.5 Å/sec with chamber pressure of approximately $1.6x10^{-4}$ Torr for drive currents ranging from 1 ampere to 3 amperes in 0.5 ampere increments. Spectral measurements were then made for these films and the moisture stability and optical properties determined.

The results obtained for the optical characterization and the moisture stability of the films is summarized in Table II. All of the terms are as defined previously for Table I.

Table II.
TiO_2 Film Data

#	D_I	CD_{avg}	n_{560}	k_{560}	$\Delta n_{3\lambda/4}$
non	0	0	2.201	0	-0.037
79	1.0	40	2.249	0.001	-0.036
80	1.5	69	2.280	0.0005	-0.029
82	2.0	101	2.328	0.0007	-0.023
87	2.5	145	2.349	<0.001	-0.003
85	3.0	187	2.488	<0.001	0

A plot of the TiO_2 moisture stability vs. the O_2 ion current density is shown in Figure 20. Note that the shape of the curve is different than that for Ta_2O_5 shown in Figure 18. The onset of improved moisture stability requires higher

ICD levels. Also note that the data for TiO_2 seems to be much better behaved. The average ICD level to make moisture stable films of TiO_2 seems to be higher than that required for Ta_2O_5 films.

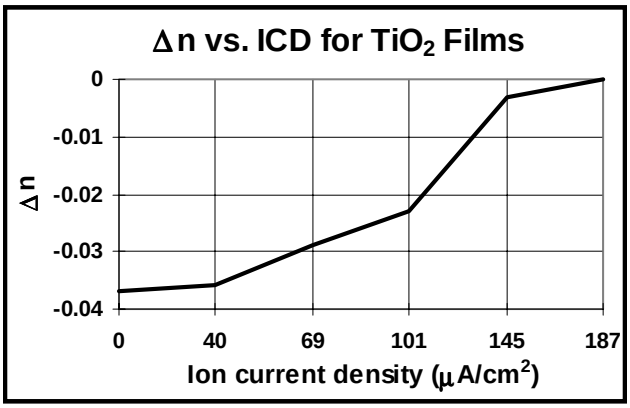

Figure 20. Moisture stability for titania (TiO_2) films

Previous work[21] reported deposition of 12 layer stacks of TiO_2, Ta_2O_5 and Nb_2O_5 deposited with SiO_2 to make 12-layer moisture stable stacks [design $(H\ L)^6$]. Plots of the wet and dry TiO_2/SiO_2 stack are shown in Figure 21.

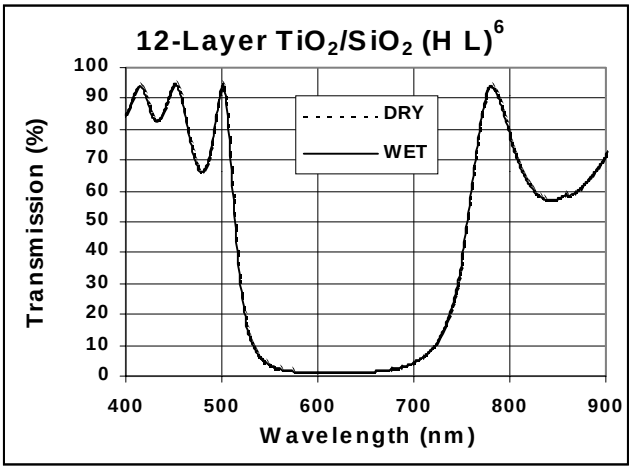

Figure 21. 12-layer TiO_2/SiO_2 $(H\ L)^6$ stack showing overlapping wet and dry scans.

PUMPING SPEED EFFECTS

Like other plasma ion guns, the CC-105 is available to be retrofitted into existing coating systems. It had become apparent over the last couple of years that integration into other systems is physically relatively easy but that directly applying our published parameters did not lead to the same results. The one factor that seemed to be different between systems was the pumping speed. Therefore we implemented a detailed study in an Integrity® 36 system where the pumping speed was varied from maximum values to lower values[21]. This study was conducted in two parts and will be summarized briefly here. The first part of the study was to determine the changes observed in the operational characteristics of the ion source as the pumping speed was reduced and the second part was to determine required deposition parameters to make good films.

The pumping speed was varied by blocking part of the pumping port between the chamber and the high vacuum pump, a cryo-pump in this example. The oxygen pumping speed for each port configuration was calculated from the relationship:

$$S = \frac{0.0127 * F}{P} \qquad (8)$$

where F is the flow in sccm and P is the pressure in Torr.

The plasma ion gun drive voltage was then measured over the entire pressure and drive current range studied previously. Complete details are contained in the original document[21]. Figures 22 and 23 show the results for $2x10^{-4}$ Torr and $3x10^{-4}$ Torr.

At 1400 l/sec the voltages required to maintain the drive current are only slightly higher for $3x10^{-4}$ Torr pressures. However the voltage for the $2x10^{-4}$ Torr curve is about 50 volts higher than for the 2350 l/sec oxygen pumping speed and the plasma cannot be sustained above 2.5 amps. The voltage increase for the $1x10^{-4}$ Torr pressure is even higher (not shown here) about 100 volts higher and the drive current cannot be sustained above 1 amp. The voltages increase even more for the 866 l/sec and 471 l/sec pumping speed configurations. Figure 22 and Figure 23 show the drive voltage vs. drive current characteristics comparison for all 4 pumping speeds for starting pressures of $2x10^{-4}$ Torr and $3x10^{-4}$ Torr respectively.

It is of some interest to note that the level of pressure increase as a function of the drive current is also greater as the pumping speed decreases. This difference is not all that noticeable at the higher pumping speeds but becomes significant at the lower pumping speed (<500l/sec).

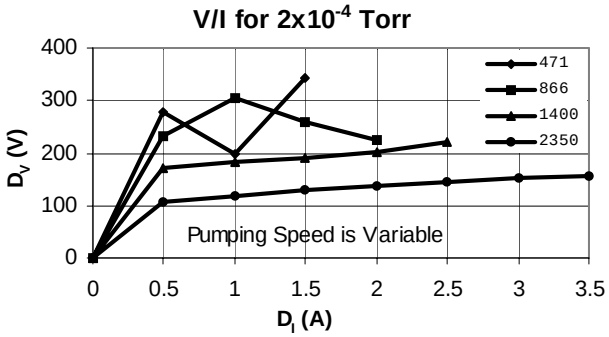

Figure 22. V/I characteristics for various pumping speeds for an initial pressure of 2 x 10^{-4} Torr.

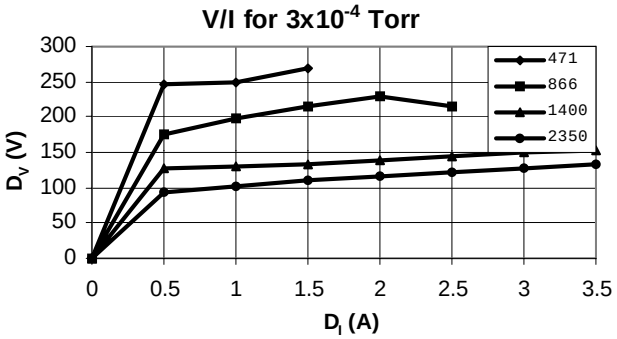

Figure 23. V/I characteristics for various pumping speeds for an initial pressure of 3 x 10^{-4} Torr.

There are some applications where higher ion energies are not desirable. Specifically where the purpose of the ion assist is to densify a coating but too much energy will break the deposited molecules apart, adversely affecting the microstructure or cause absorption. Therefore establishing a lower drive voltage can be desirable. The increased drive voltage required to sustain plasmas at lower pumping speeds is not necessarily good. One way to offset the voltage increase is to increase the oxygen flow that gives a higher pressure and a lower voltage. The important factor is the characteristic of the films that can be made by depositing in systems with various pumping speeds.

A different Integrity® -36 coating chamber was used to deposit TiO_2 films using different pumping speeds. Therefore the actual pumping speeds will vary for this data from those presented in the data above. The purpose of this effort was to determine which changes in the process were necessary to make good films at different pumping speeds. Also, if good films could not be made, how bad were they?

The TiO_2 films were deposited to 3000 Å at 3.5 Å/sec using an ambient substrate temperature (typically starting at 50 ºC and ending at approximately 85 ºC). The base pressure before introducing oxygen through the ion source was 7 x 10^{-6} Torr for the higher pumping speeds and was <2 x 10^{-5} Torr for the lower pumping speeds. All runs were done with a 2 ampere drive current (the drive voltage varied to maintain the current). The oxygen flow rate was used as a variable to control the optical properties of the films (refractive index and extinction coefficient).

Films were deposited using four pump speeds (1800, 1200, 960 and 600 l/sec) and flow rates of 13.3, 17.3, 21.3 and 25.3 sccm as needed to achieve non-absorbing thin films which were moisture stable and a film which was not moisture stable. The range of conditions run and the refractive index of the films (@ 560 nm) are plotted in Figure 24.

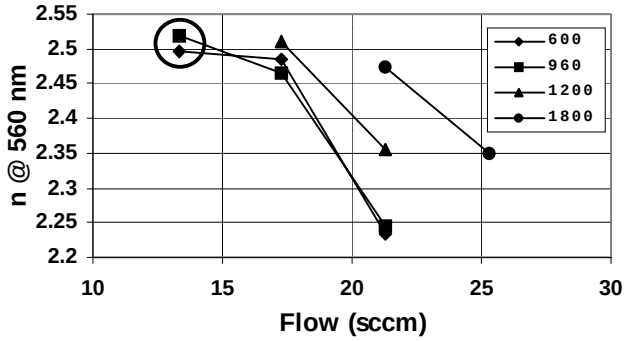

Figure 24. n vs. flow for TiO_2 films prepared at different pumping speeds. Circled values have k > .001 at 560 nm.

All of the above films with a refractive index > 2.46 are moisture stable. All of the films with a refractive index of < 2.45 are not moisture stable. Both of the films deposited at 13.3 sccm have k (extinction coefficients) > .001 at 560 nm. Also, the films deposited using a 13.3 sccm flow resulted in a deposition pressure that was too low to maintain the 2 ampere drive current. For these films the drive current was reduced to about 1.4–1.5 ampere, was erratic and the drive voltage was 800 volts. The drive voltage for all of the other films ranged from 220 volts to 300 volts. The films prepared using a flow of 17.3 sccm and higher were basically non-absorbing.

The above data is consistent with data we have reported previously. That is, the refractive index of the film increases as the oxygen pressure (flow) decreases. The interesting factor that comes out of this study is that the transition to higher index takes place at higher flow rates for the higher pumping speeds. This, of course, is not totally unexpected since we already know that the higher the pressure during deposition, the lower the film index, all other things being equal. However, what does change at different pumping speeds is the effect of the gettering action on the pressure during deposition. This effect is shown in Figures 25 (pressure) and Figure 26 (pressure change – gettering).

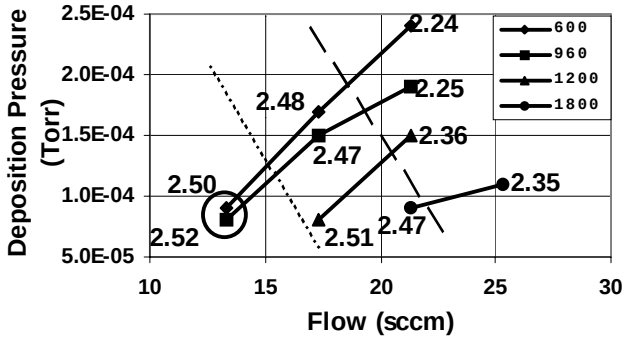

Figure 25. Pressure while depositing TiO_2. Refractive index at 560 nm shown with each data point.

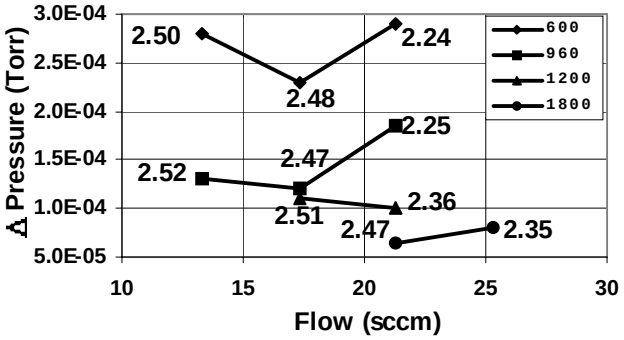

Figure 26. Oxygen pressure change (gettering) during TiO_2 deposition using various oxygen flow rates and chamber pumping speeds.

In Figure 25 the region to the left and below the dotted line show films which were absorbing. The region between the dotted and dashed line are films which are moisture stable. The region to the right and above the dashed line is films that are not moisture stable.

From Figure 26 we can see that at each pumping speed the change in pressure due to gettering is about the same (indicating that the same amount of oxygen is being used up) regardless of input flow. However, the change of pressure due to gettering increases as the pumping speed decreases.

All of the refractive index dispersion curves have about the same shape. This is shown in Figure 27. containing curves for 8 of the films prepared for this study are plotted, two for each of the pumping speeds (solid line for moisture stable sample and dotted line for the sample which is not moisture stable).

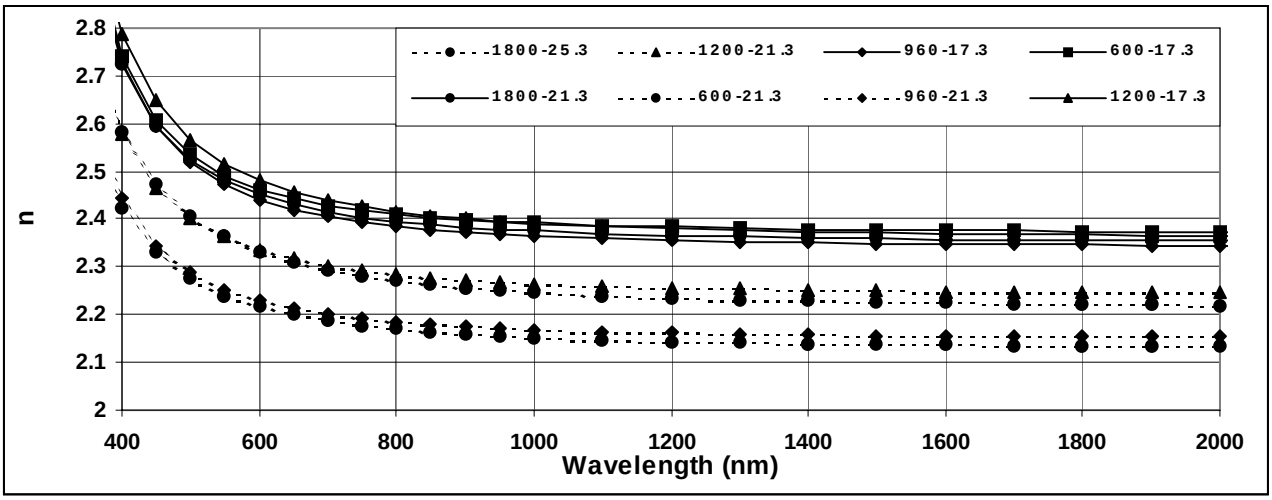

Figure 27. Dispersive refractive index of various films. the first # is pumping speed (l/sec) and second # is O_2 flow (sccm).

REFERENCES

1) W. Essinger (1992) *Ion sources for ion beam assisted thin-film deposition* Rev. Sci. Instrum. **(63)** 11-5217.
2) James T. McNally (1986) Report No. AFIT/CI/NR 86-77D (Dissertation at Univ. of New Mexico).
3) John R. McNeil, Alan C. Barron, S. R. Wilson and W. C. Herrmann Jr. (1984) *Ion-assisted deposition of optical films: low energy vs high energy bombardment* Applied Optics **(23)** 4-552.
4) John R. MaNeil, G. A. Al-Jumaily, K. C. Jungling and A. C. Barron (1985) Applied Optics *Properties of TiO_2 and SiO_2 thin films deposited using ion assisted deposition* Applied Optics **(24)** 4-486.
5) John R. McNeil and W. C. Herrmann Jr. (1982) *Ion beam applications for precision infrared optics* J. Vac. Sci. Technol. **(20)** 3-324.
6) T. Spalvins (1980) *Survey of ion plating sources* J. Vac. Sci. Technol. **(17)** 1-315.
7) F. Flory, G. Albrand, C. Montelymard and E. Pelletier (1986) *Optical studies of the growth of Ta_2O_2 and SiO_2 layers obtained by ion assisted deposition* SPIE Vol. 652 Thin Film Technologies II - 248.
8) P. J. Martin, R. D. Netterfield and W. G. Sainty (1984) *Modification of the structural properties of dielectric ZrO_2 films by ion-assisted deposition* Applied Physics **(55)** 1-235.
9) Steven G. Saxe, M. J. Messerly, Bertrand Bovard, Lewis, DeSandre, Fred J. Milligen and H. A. Macleod (1984) *Ion bombardment-induced retarded moisture adsorption in optical thin films* Applied Optics **(23)** 20-3633.
10) P. J. Martin, H. A. Macleod, R. P. Netterfield, C. G. Pacey and W. G. Sainty (1983) *Ion-beam-assisted deposition of thin films* Applied Optics **(22)** 1-178.
11) O. Zabeida, J. E. Klemberg Sapieha, L. Martinu and D. E. Morton (1999) *Ion Bombardment Characteristics During the Growth of Optical Films Using a Cold Cathode Ion Source* 42nd Annual Technical Conference Proceedings of the SVC, p 267.

12) O. Zabeida and L. Martinu, J. Appl. Phys., **85**(9), p. 6366, 1999**.**
13) O. Zabeida, J.E. Klemberg-Sapieha, L. Martinu, and D. Morton, Proc. 1998 Fall Meeting, Materials Research Society, Boston, 1998.
14) A. Hallil, O. Zabeida, J.E. Klemberg-Sapieha, M. Wertheimer, and L. Martinu (1999) *Mass Resolved Ion Energy Distribution in Dual-Mode Microwave/Radio Frequency Plasma* Proc. 42 Ann. Tech. Conf., Society of Vacuum Coaters, Chicago p 311
15) J.R. McNeil, J.J. McNally and P.D. Reader (1988) *Ion Beam Deposition*, in Handbook of Thin-Film Deposition Processes and Techniques, Ed. by Klaus K. Schuegraf, Noyes Publications, p 369.
16) D. E. Morton, V. Fridman, (1998) *Measurement and Correlation of Ion Beam Current Density to Moisture Stability of Oxide Film Stacks Fabricated by Cold Cathode Ion Assisted Deposition* Proc 41 Annual Technical Conference of the SVC, Boston p 297.
17) H. A. Macleod, Thin Film Optical Filters, 2nd Ed. (Macmillean Publishing Co., New York 1986) pp. 370-373.
18) L. Martinue, in Plasma Processing of Polymers, Kluwer Academic Publishers, Dordrecht, 1997, p 247.
19) J.J. Cuomo, S.M. Rossnagel, and H.R. Kaufman, ed., Handbook of Ion Beam Processing Technology, Noyes Publications, Park Ridge, NJ, 1989.
20) S.M. Rossnagel, J.J. Cuomo, and W.D. Westwood, ed., Handbook of Plasma Processing Technology, Noyes Publications, Park Ridge, NJ, 1989.
21) D. E. Morton (2000) *The Effect of Pumping Speed on the Operation of a Cold Cathode Ion Source* Proc 43 Annual Technical Conference of the SVC, Denver p 207.